

## Article

# Effect of Erbium Micro-Additions on Microstructures and Properties of 2024 Aluminum Alloy Prepared by Microwave Sintering

Tao Qin <sup>1,\*</sup>, Bowen Fan <sup>1</sup>, Jincheng Yu <sup>1</sup>, Chengwei Bu <sup>1</sup> and Jiukun Zhang <sup>2</sup><sup>1</sup> School of Mechanical Engineering, Wuxi Institute of Technology, Wuxi 214121, China<sup>2</sup> Wuxi Wanling High Frequency Equipment Manufacturing Co., Ltd., Wuxi 214100, China

\* Correspondence: qint@wxit.edu.cn

**Abstract:** The effects of rare earth erbium (Er) micro-additions on the microstructures and mechanical properties of 2024 aluminum alloy were investigated. The microstructures and fracture surfaces of specimens prepared via high-energy ball milling, cold isostatic pressing and microwave sintering were carried out by optical microscopy (OM) and scanning electron microscopy (SEM). Under the conditions of sintering heating rate of 20 min/°C and soaking time of 30 min at 490 °C, it was found that with the increase in Er addition, the grain size first decreased then increased, and it reached a minimum size of about 5 μm when the Er content was 0.6%, showing that the grains were refined. At the same time, the compactness and microhardness reached maximum levels, which were 97.6% and 94.5 HV, respectively. Moreover, the tensile strength and elongation reached the peak at 160.5 MPa and 4.4%, respectively. The dynamic mechanical response of Er/2024Al alloy with different Er content was studied through a split Hopkinson pressure bar (SHPB) at strain rates of 600 s<sup>-1</sup> and 800 s<sup>-1</sup>, respectively. Both at the strain rates of 600 s<sup>-1</sup> and 800 s<sup>-1</sup>, the dynamic yield stress of the specimens increased gradually with an increase in Er content. For the 0.6 wt.% Er specimen, the dynamic yield stress reached 371.3 MPa at a strain rate of 800 s<sup>-1</sup>, which was 28.2% higher than that at a strain rate of 600 s<sup>-1</sup>. When the strain rate is 800 s<sup>-1</sup>, the deformation degree of the 0.6 wt.%Er specimen is 55.3%, which is 14.7% higher than for the Er-free one, and there are adiabatic shear bands formed in the 0.6 wt.%Er specimen. Through a fracture analysis of the samples, a certain number of dimples appeared in the fracture of an impact specimen, indicating that the addition of Er improved the toughness of the material. This research can provide a reference for the development and application of high-performance aluminum alloy in automotive structural materials.

**Keywords:** Er; microwave sintering; microstructure; mechanical properties; split Hopkinson pressure bar



**Citation:** Qin, T.; Fan, B.; Yu, J.; Bu, C.; Zhang, J. Effect of Erbium Micro-Additions on Microstructures and Properties of 2024 Aluminum Alloy Prepared by Microwave Sintering. *Crystals* **2024**, *14*, 382. <https://doi.org/10.3390/cryst14040382>

Academic Editor: Shouxun Ji

Received: 19 March 2024

Revised: 11 April 2024

Accepted: 17 April 2024

Published: 19 April 2024



**Copyright:** © 2024 by the authors. Licensee MDPI, Basel, Switzerland. This article is an open access article distributed under the terms and conditions of the Creative Commons Attribution (CC BY) license (<https://creativecommons.org/licenses/by/4.0/>).

## 1. Introduction

2024 aluminum alloy (2024Al) belongs to the aluminum–copper–magnesium series. Its composition is well balanced and possesses good comprehensive mechanical properties. It is the most widely used aluminum alloy of the 2 series aluminum alloys, it is widely used in aviation (such as in aircraft engines, structural parts, wings, etc.), power machinery, electronics, automobile manufacturing, and other fields [1,2], and it is one of the most ideal lightweight structural materials. In the 2024 aluminum alloy, Cu and Mg are the main alloying elements. In addition, there is a small amount of Mn and trace amounts of Si and Fe. The preparation methods of the alloy mainly include fusion casting and powder metallurgy. The advantages of the melt casting method are its simple process, low cost, and the ability to prepare castings with complex shapes. However, during preparation, there are inevitably defects such as component segregation, coarse grains, and interfacial reaction, etc. [3]. Being a new powder metallurgy method, microwave sintering (MWS) can effectively avoid composition segregation, reduce interfacial reactions, promote the

uniform distribution of reinforcements, refine grains, and improve solid solubility [4]. Microwave sintering has become the main method to prepare high-performance aluminum alloys [5–8].

The energy crisis and the increasingly severe environmental protection situation have put forward higher requirements for lightweight high-performance structural materials. Rare earth elements have special physical and chemical activities and can be used as an ideal adding phase. Adding an appropriate amount of rare earth elements can refine the grain, optimize the structure, and eliminate impurities, and, furthermore, it can improve the comprehensive mechanical properties of alloys or composites [9,10]. As the most widely used high-strength lightweight material, the 2024 aluminum alloy is generally added with alloying elements to improve its microstructure and mechanical properties, and the addition of rare earth elements and their oxides has been proven to be one of the most effective methods. There are three strengthening mechanisms of rare earth elements in aluminum alloy or matrix composites: solid solution strengthening, fine grain strengthening, and dispersion strengthening [11].

In recent years, researchers have tried to explore the effects of different rare earth elements on the microstructures and mechanical properties of aluminum alloys. In 2009, TSAI Y C et al. [12] tried to add a certain amount of La into the A356 aluminum alloy. When the content of La was greater than 0.6%, the breaking elongation of the alloy was significantly improved, and when the content of La reached 1.0%, the eutectic Si phase in the alloy changed from coarse slats to short fibers. In 2019, Zhong Tao et al. [13] added a small amount (0.35 wt.%) of Ce to the 3003 aluminum alloy, and the micro Vickers hardness (HV) of the alloy obtained was 56.3 HV higher than that without Ce. In 2019, Ding W W et al. [14] added the Al-10Y alloy to the 6063 aluminum alloy, and the grain of the modified alloy was obviously refined, and the microstructure became more uniform. Studies have shown that an appropriate amount of rare earth Er has a good modification effect on the eutectic Al-Si alloy, and the addition of Er improves the mechanical properties of hypoeutectic aluminum alloy more than that of rare earth La [15,16]. The rare earth Er is another effective microalloying element besides Sc in aluminum alloys [17,18], and its price is relatively low. A micro amount of Er can generate fine and dispersed  $\text{Al}_3\text{Er}$  particles in Al-Mg, Al-Mn, and Al-Zn-Mg alloys, which can effectively stabilize the substructure, inhibit recrystallization, and improve the comprehensive properties of the alloy [19]. On the premise of keeping the breaking elongation of the alloy unchanged, a small amount of Er addition can not only greatly improve the room temperature strength of pure aluminum and aluminum magnesium alloys, but can also increase the recrystallization temperature of the alloy, which is conducive to an improvement in high-temperature properties.

At present, the research on rare earth reinforced aluminum alloy mainly focuses on the fusion casting method, and on the mechanism of Y, Ce, La, and their mixtures in aluminum alloy and aluminum matrix composites. Compared to other rare earth elements such as Y, Ce, and La, the price of the rare earth element Er is more affordable, yet it has similar effects in enhancing the mechanical properties of aluminum alloys. This makes it more attractive economically. In addition, the research on adding rare earth elements to aluminum matrix composites prepared by microwave sintering is less. Different from traditional sintering methods, microwave sintering has the characteristics of uniform temperature, fast low-temperature sintering, and selective sintering. Therefore, it is necessary to explore the process of preparing a rare earth aluminum alloy by microwave sintering to further improve the properties of the aluminum alloy and its composites and develop new aluminum matrix composites. In this paper, the 2024Al-Er alloy was prepared by high energy ball milling, cold isostatic pressing, and microwave sintering, the effect of Er on the microstructure and mechanical properties was studied, and the mechanism by which the addition of Er affects the microstructure and performance of the alloy was discussed; in particular, the dynamic mechanical properties of the 2024Al-Er alloy were analyzed in detail, which provided a feasible idea for the preparation and development of a high-performance aluminum alloy.

## 2. Experimental Details

Commercial powders of 2024Al and Er were used as raw materials for the experiment. The particle size of the 2024Al powder was below 5  $\mu\text{m}$  and that of the Er powder was below 40  $\mu\text{m}$ . The morphologies of the two original powders are shown in Figure 1, and the chemical composition of 2024Al and the experimental scheme for preparing the new 2024Al-Er alloy are shown in Tables 1 and 2.

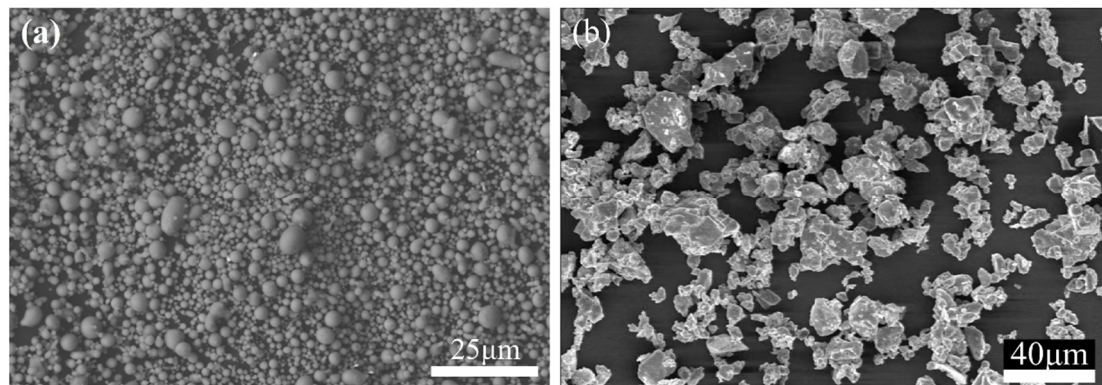


**Figure 1.** Morphology of the original powder: (a) 2024Al and (b) Er.

**Table 1.** The chemical composition of 2024Al (wt.%).

Element	Al	Cu	Mg	Mn	Si	Fe	Cr	Zn	Ti	Others
Content	Residual	3.8–4.9	1.2–1.8	0.3–0.9	$\leq 0.5$	$\leq 0.5$	$\leq 0.1$	$\leq 0.25$	$\leq 0.15$	$\leq 0.15$

**Table 2.** Experimental plan for the preparation of 2024Al-Er alloy (wt.%).

Serial No.	2024Al	Er
0	100.0	0
1	99.8	0.2
2	99.6	0.4
3	99.4	0.6
4	99.2	0.8

Firstly, the two powders were mixed according to the proportion of ingredients and then placed into the high-energy ball milling machine for ball milling. The ball milling process parameters are shown in Table 3.

**Table 3.** The ball milling process parameters.

Parameters	Level
Milling time	5 h
Alcohol-to-powder material ratio	2:3
Balls-to-materials ratio	5:1
Large balls-to-medium balls-to-small balls ratio	1:2:4

After high-energy ball milling, the evenly mixed powder was placed in a vacuum-drying oven at 60  $^{\circ}\text{C}$  for 72 h. Then, the dried powder was filled into the rubber mold, which was put into the cold isostatic press machine. The rubber mold filled with mixed powder could withstand a pressure of 300 MPa for 2 min. The pressed green bodies were sintered in the microwave sintering equipment with argon protection. The optimized microwave sintering process is demonstrated in Table 4.

**Table 4.** The technological parameters of microwave sintering process.

Parameters	Level
Output power	4 kW
Frequency	2.45 GHz
Heating temperature	490 °C
Heating rate	20 °C/min
Soaking time	30 min

The sintered specimens for microstructure observations were mechanically polished and then etched using Kohler reagent (2.5% HNO<sub>3</sub> + 1.5% HCl + 1% HF + 95% H<sub>2</sub>O). The microstructures of the specimens were observed by the S-3400 N scanning electron microscope (SEM), and the phase analysis was performed using a D8 ADVANCE X-ray diffractometer (XRD) (BRUKER AXS GMBH, Karlsruhe, Germany).

The compactness of the 1 cm × 1 cm × 1 cm block was obtained in the experiment by means of the Archimedes principle. The actual density of the specimen can be calculated using Equation (1):

$$\rho = \frac{m_1}{m_1 - m_2} \cdot \rho_{water} \quad (1)$$

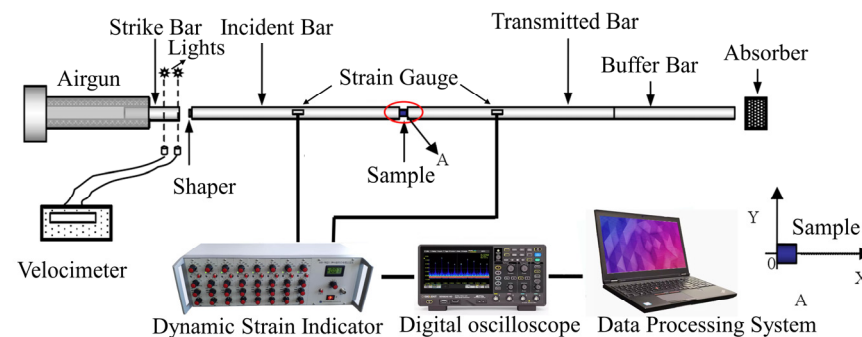
where  $\rho$  is the density of the specimen,  $\rho_{water}$  the density of distilled water used in the experiment,  $m_1$  is the mass of the dry specimen, and  $m_2$  is the mass of the specimen in the distilled water. The full density  $\rho_0$  of the alloy can be calculated using Equation (2):

$$\rho_0 = \sum \rho_i \cdot v_i \quad (2)$$

where  $\rho_i$  is the theoretical density of  $i$  phase, and  $v_i$  is the volume fraction. Then, the compactness  $I$  can be calculated from Equation (3):

$$I = \frac{\rho}{\rho_0} \quad (3)$$

The dynamic compressive properties of the specimens were tested by the split Hopkinson pressure bar (SHPB). A schematic illustration of the SHPB system is presented in Figure 2. Cylindrical specimens of 8 mm diameter and 6 mm height were prepared for SHPB experiments. The specimens after a dynamic impact test were cut along the axial direction. After grinding, polishing, and etching, the microstructure changes after deformation were analyzed by OM and SEM. Moreover, the fracture morphology was observed. The effect of different Er additions on the impact deformation and failure behavior of the alloy was studied.

**Figure 2.** Schematic representation of split Hopkinson pressure bar (SHPB) system.

### 3. Results and Discussion

#### 3.1. Microstructure

Figure 3 presents the SEM micrographs of the 2024Al-Er alloy with different Er contents: 0% (Figure 3a), 0.2 wt.% (Figure 3b), 0.4 wt.% (Figure 3c), 0.6 wt.% (Figure 3d), and

0.8 wt.% (Figure 3e). The Er-containing specimens showed changes in microstructure in comparison to the Er-free one.

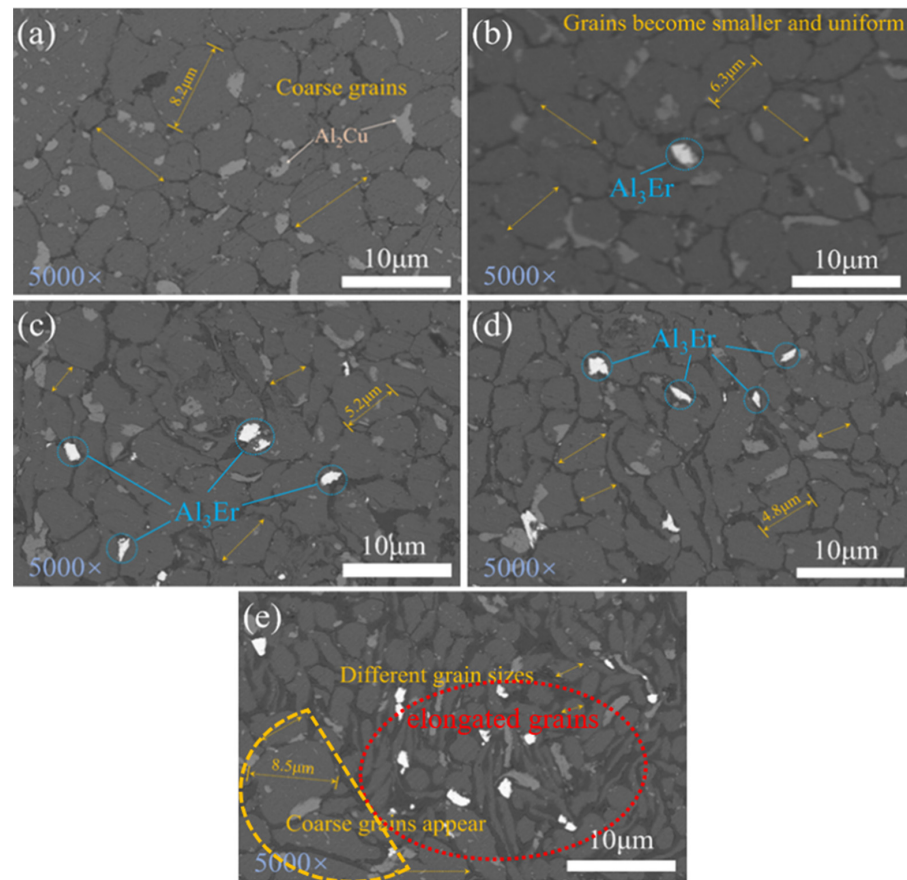


**Figure 3.** The SEM micrographs of 2024Al-Er alloy with different Er content: (a) Er-free, (b) 0.2 wt.%, (c) 0.4 wt.%, (d) 0.6 wt.%, and (e) 0.8 wt.%.

Firstly, the grain size of the specimens changed. The grain size of the Er-free specimen is large and inhomogeneous, and the diameter of large grains is about 8  $\mu\text{m}$ . With the increase in Er content, the grain size decreases gradually. When Er content is 0.6 wt.%, the average grain diameter is less than 5  $\mu\text{m}$ . The grain size is significantly refined, and the grain shape is relatively smooth. The grain refinement in the 2024 aluminum alloy is mainly due to the addition of Er, which reacts with the Al in the matrix and generates fine  $\text{Al}_3\text{Er}$  particles dispersed on the 2024Al matrix. These fine  $\text{Al}_3\text{Er}$  particles can pin the dislocation and sub-grain boundary of the composite, and hinder the recombination of the dislocations and the migration of the sub-grain boundary, thus delaying the nucleation and growth of the grains and playing a role in refining grains. This is similar to previous research, which has shown that Er and Al can form an  $\text{Al}_3\text{Er}$  compound. This compound has a high melting point and shares the same crystal structure as the aluminum matrix, making it suitable as a core for heterogeneous nucleation [20,21].

Secondly, the substitutional solid solution can be formed when Er is dissolved in the 2024Al matrix, which can fill the defects on the surface of the alloy phase, and it is also conducive to improving the nucleation rate, which is an important means of grain refinement. Moreover, during microwave sintering, Er can interact strongly with impurity elements Si and Fe in the 2024Al alloy, preventing them from entering the solid solution. Therefore, Er also has a certain purification effect on the grain boundary of the 2024Al alloy and can improve the toughness of the aluminum alloy [22].

When the Er content reaches 0.8 wt.% (Figure 3e), the grain size is uneven, with coarse elongated grains coexisting with fine ones and also including some coarse equiaxed grains.

Such anisotropy in grain size and shape is detrimental to the mechanical properties of the alloy. According to the literature, it can be inferred that the content of Er is high, forming inclusion  $\text{Al}_3\text{Cu}_4\text{Er}$  [23], and the refining effect is weakened.

Figure 4 presents the microstructure of the 2024Al-Er alloy obtained by SEM and the EDS mapping of the typical region of the 0.6 wt.% Er alloy. The EDS energy spectrum analysis was performed on the spot marked in Figure 4a, and the results show that the ratio of the atomic numbers of Al and Er is about 3:1 (Figure 4f), which can be deduced to be the  $\text{Al}_3\text{Er}$  phase [24]. In Figure 4d, the content of the Er element in the marked area is obviously larger, which corresponds to  $\text{Al}_3\text{Er}$  phases (Figure 4a), while there is a certain amount of Er in other areas, and the distribution is relatively uniform. On the one hand, Er dissolved in the 2024 aluminum alloy matrix can form a substitutional solid solution, which plays a role in solution strengthening; on the other hand, Er and Al form a fine compound  $\text{Al}_3\text{Er}$ , which is dispersedly distributed in the 2024Al matrix. The distribution of Cu (Figure 4c) is relatively uniform, and there will be some elements gathered in a small range, mainly the  $\text{Al}_2\text{Cu}$  phase in the 2024 aluminum alloy.

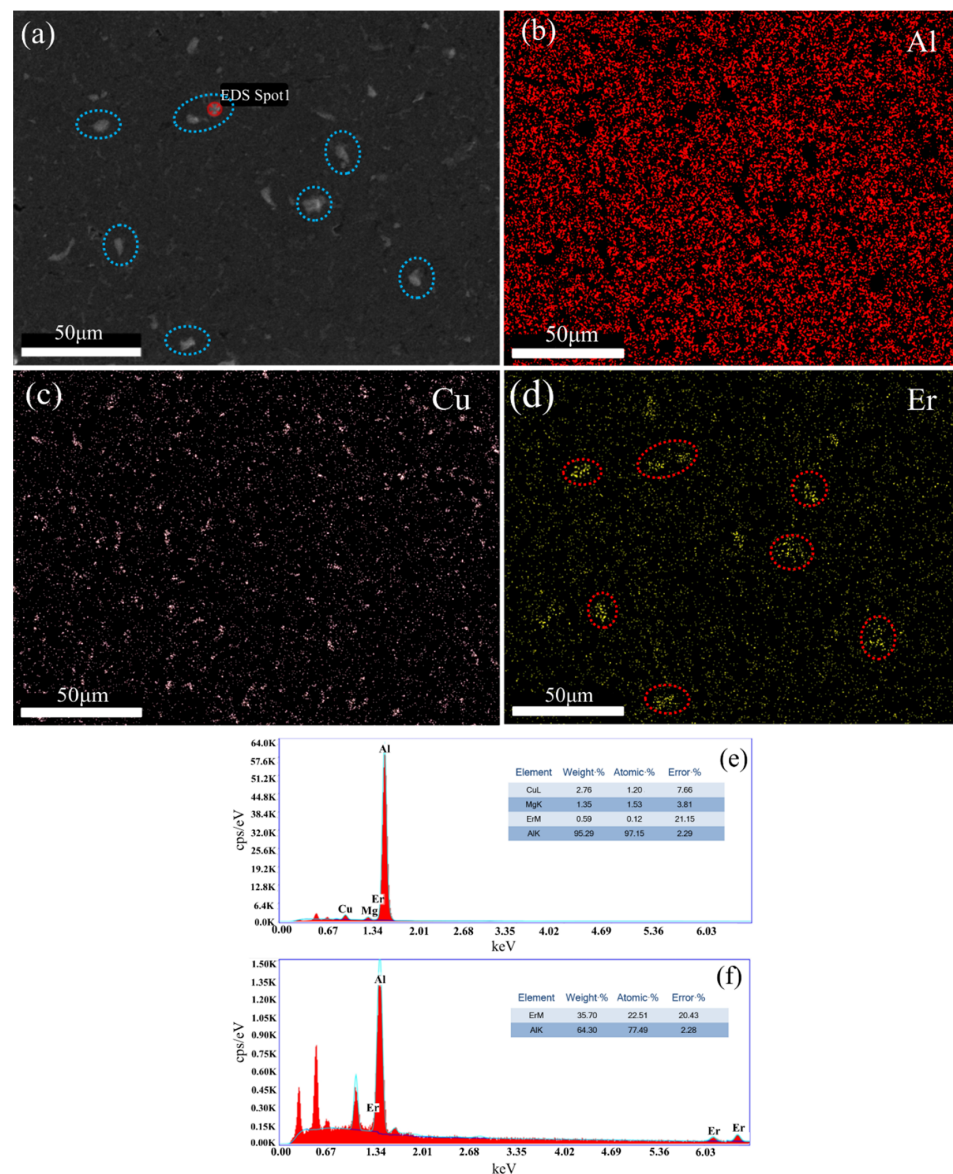


**Figure 4.** The microstructure of the 2024Al-Er alloy obtained by SEM and EDS mapping of the typical region of the 0.6 wt.% Er alloy: (a) overall view map; (b) Al; (c) Cu; (d) Er; (e) element composition of (a); and (f) element composition at spot 1.

### 3.2. XRD Analysis

Figure 5 shows the XRD patterns of the 2024Al-Er alloy with different Er contents. For the Er-free alloy, the XRD patterns of the specimen are only Al and Al<sub>2</sub>Cu. As Er is added, the diffraction peak of Al<sub>3</sub>Er appears, and its intensity increases with an increase in Er content, indicating that the number of the Al<sub>3</sub>Er phase increases. That is to say, the addition of the Er element to the alloy does not completely exist in a solid solution form in the matrix. Part of it will be dissolved in the Al matrix for solid solution strengthening, while the other part will precipitate in the form of a fine Al<sub>3</sub>Er phase for dispersion strengthening. Moreover, the diffraction peak of Al<sub>8</sub>Cu<sub>4</sub>Er is not obvious, mainly because its content is relatively low and difficult to detect. This is consistent with the change trend of the microstructure in Section 3.1.

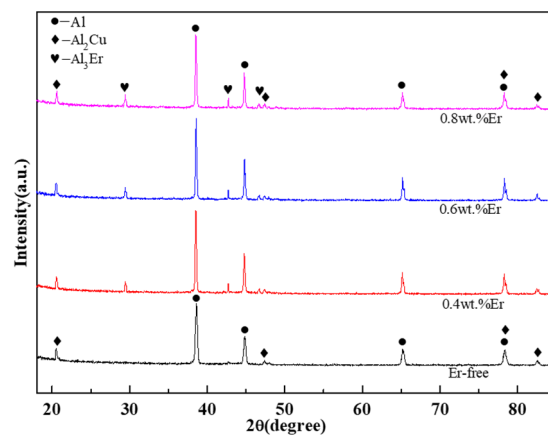


**Figure 5.** XRD pattern of 2024Al-Er alloy.

### 3.3. Compactness and Microhardness

Figure 6 shows the effect of Er content (0%, 0.2 wt.%, 0.4 wt.%, 0.6 wt.%, 0.8 wt.%) on the compactness and microhardness of the 2024Al-Er alloy. It can be seen that the Er content has a significant effect on the compactness of the alloy. When Er is not added, the compactness of the alloy is 95.7%. With the increase in Er addition (0.2 wt.% → 0.4 wt.% → 0.6 wt.% → 0.8 wt.%), the compactness increases first and then decreases. When the Er content is 0.6 wt.%, the highest compactness arrived is 97.6%. The change in compactness mainly depends on the interaction between the matrix and reinforcing phase. During the sintering process, with an increase in Er content, the content of the Al<sub>3</sub>Er phase in the matrix increases, which will enhance the ability to absorb and convert microwaves, and produce more heat, which can cause the green-body rapid heating process, and lead to a more uniform structure and higher compactness. When the Er content is 0.8%, the compactness of the alloy decreases. It is regarded, through analysis, that an interaction occurred between Er and Al, and Cu in the 2024Al matrix, meaning the Al<sub>8</sub>Cu<sub>4</sub>Er phase with a low melting point is formed, and closed pores are generated in a local range, making the gas difficult to discharge [25–27]. On the other hand, due to the strong enrichment ability of rare earth Er in the matrix, most of the rare earth Er will gather at the junction of the two-phase interface. Excessive rare earth Er will cause the matrix to split locally, which will deteriorate the region and make the overall mechanical properties decrease instead.

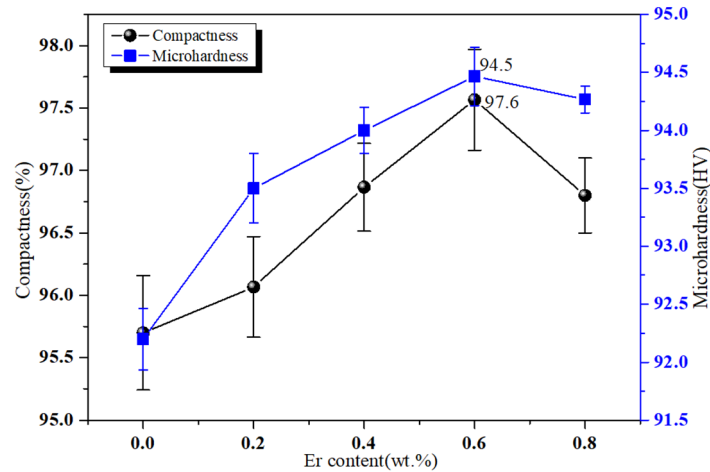


**Figure 6.** Dependence of compactness and microhardness of 2024Al-Er alloy with different Er content.

As shown in Figure 6, with the increase in Er content, the microhardness first increases and then decreases. When the addition of Er is 0.6%, the microhardness reaches the maximum, which is 94.5 HV, 2.5% more than for the Er-free specimen. The reason for the microhardness increase in the 2024Al-Er alloy is that Er, as a heterogeneous atom dissolved in the matrix, causing lattice distortion in the matrix, and the potential barrier of the distorted lattice increases and the ability to resist deformation increases. From the perspective of microstructure, with the increase in Er addition, the number of the second phase in the material increases, and the grain boundary increases. The dislocations on the grain boundary intertwine with each other, forming a large number of defects, leading to an improvement in the deformation resistance and hardness of the alloy. When the addition of Er reaches 0.8 wt%, the hardness decreases. This is largely due to excessive Er reacting with Cu in 2024Al to form low-melting-point  $Al_3Cu_4Er$  phases, which would cause more pores in the structure, lower compactness, and lower hardness. Wang [28] studied the effect of densification in the 2024Al alloy reinforced with high-entropy alloy (HEA) particles of FeCoNi1.5CrCu. The initial compactness of the pure 2024Al alloy was 94.6%. Upon the introduction of the HEA particles, the maximum achieved compactness was 90.8%, and the maximum microhardness of FeCoNi1.5CrCu/2024Al composite material was 93.1 HV. This indicates that under the same preparation conditions, the effect of improving Er alloying on compactness and hardness is better than that of FeCoNi1.5CrCu HEA particles.

### 3.4. Tensile Properties

Figure 7 shows the tensile properties of the 2024 aluminum alloy under different Er contents. It can be concluded that with the increase in Er addition, the strength and plasticity of the alloy are both improved. When the addition of Er is 0.6 wt.%, it reaches its peaks at 160 MPa and 4.5%, respectively. According to Figure 3, we can see that when the addition of Er is less than 0.6 wt.%, the grain size of the 2024 aluminum alloy is significantly refined and equiaxed, producing fine grain strengthening. As is well known, grain refinement is beneficial for both the strength and plasticity of materials. If the Er addition continues to increase, the tensile strength and elongation decrease instead. On the one hand, the grain size of the alloy becomes uneven, which affects the mechanical properties of the material; on the other hand, when the amount of Er added exceeds 0.6 wt.%, in addition to the formation of the  $Al_3Er$  phase, a portion of the AlCuEr phase may be formed, which reduces the mechanical properties of the alloy. Lei added Er to an Al-Si-Mg-Cu alloy and also found that the addition of 0.6 wt.% erbium has a greater promotion effect than an inhibition effect, and the alloy has the best mechanical properties at as-cast and heat-treatment conditions [29].

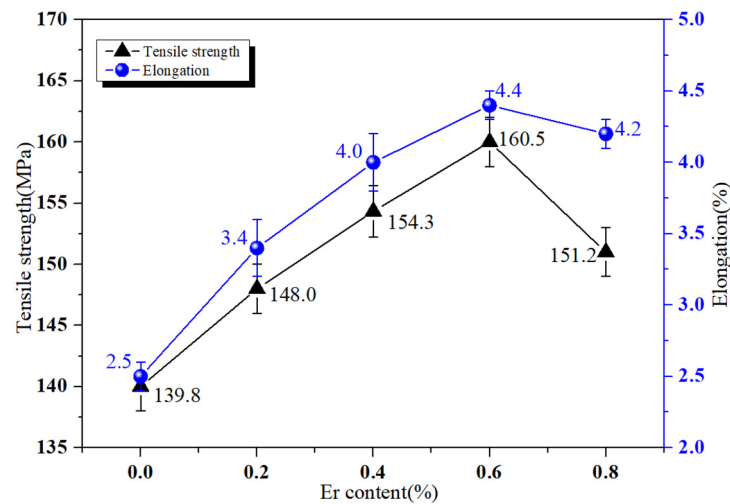


**Figure 7.** Dependence of tensile strength and elongation of 2024Al-Er alloy on different Er contents.

### 3.5. Dynamic Compression Properties

The dynamic compressive properties of the specimens were carried out on the split Hopkinson pressure bar (SHPB), as shown in Figure 2. The SHPB experimental device is mainly composed of two equal-length pressure bars, a short impact bar, and a set of impact loading devices. The strain ( $\varepsilon_s(t)$ ), strain rate ( $\dot{\varepsilon}_s(t)$ ), and dynamic stress ( $\sigma_s(t)$ ) of the specimen are calculated from Equations (4)–(6) [30]:

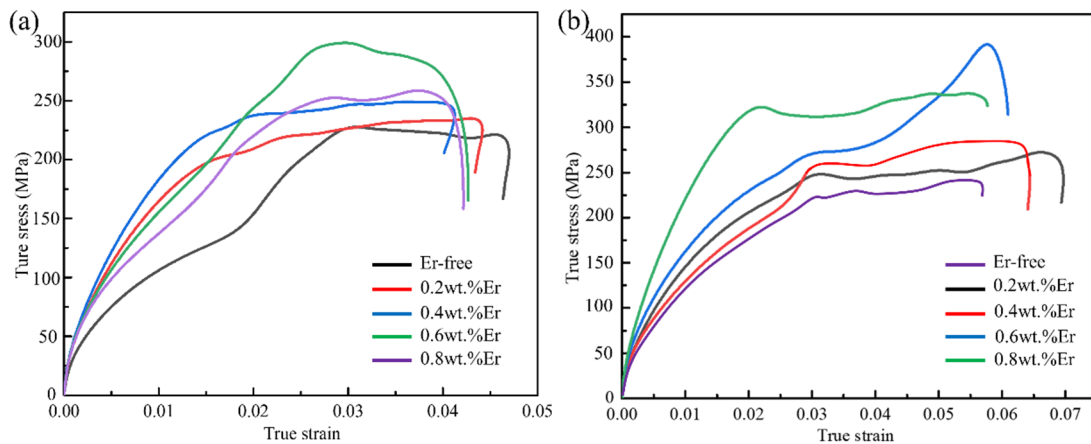
$$\varepsilon_s(t) = -\frac{2C}{L} \int_0^t \varepsilon_R(t) dt \quad (4)$$

$$\dot{\varepsilon}_s(t) = -\frac{2C}{L} \varepsilon_R(t) \quad (5)$$

$$\sigma_s(t) = E \frac{A}{A_0} \varepsilon_T(t) \quad (6)$$

where  $C$  and  $E$  are the elastic wave velocity and elasticity modulus of the pressure bar, respectively;  $L$  is the length of the specimen before impact;  $A_0$  and  $A$  are cross-sectional areas of pressure bar and the specimen before impact; and  $\varepsilon_R(t)$  and  $\varepsilon_T(t)$  are the obtained reflected and transmitted waves, respectively.

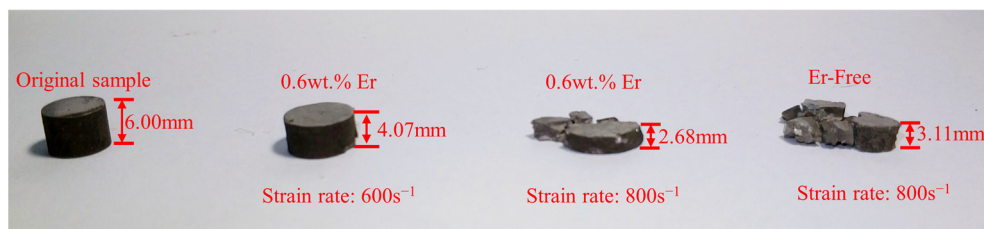
Figure 8 are the dynamic compression stress–strain curves of the 2024Al-Er alloy with different Er additions at strain rates of  $600 \text{ s}^{-1}$  and  $800 \text{ s}^{-1}$ . It can be learned that the stress–strain curves of the alloy are divided into elastic and plastic sections, each of which has obvious characteristics, and there is no obvious yield platform. True stress–strain curves at both strain rates show a wave-like response after yielding, indicating that dynamic recovery and dynamic recrystallization of the alloy occur. This is consistent with Xie’s research, which indicates that for the  $\text{SiC}_p/2024\text{Al}$  composite, during the elastic phase, the influence of different strain rates on the elastic modulus of the composite is negligible; during the plastic phase, as the strain rate increases, the yield flow stress becomes larger, and the trend of strain hardening remains roughly the same. [31]. Upon analyzing the dynamic impact of plastic deformation, it is seen that the dynamic recovery caused by the slip of the cross spiral dislocation and the edge dislocation is limited, and the subgrain boundary is not significantly formed. The dislocation density remains high, resulting in a rapid increase in energy storage. When the storage energy of the deformed metal reaches a critical value, dynamic recrystallization occurs [32]. In addition, under the condition of high strain rate, the flow stress of the alloy has a certain fluctuation, which is caused by the inertial dispersion effect and external interference that the SHPB is difficult to avoid.



**Figure 8.** True stress–true strain curves obtained from the specimens with different Er content: (a)  $600\text{ s}^{-1}$  and (b)  $800\text{ s}^{-1}$ .

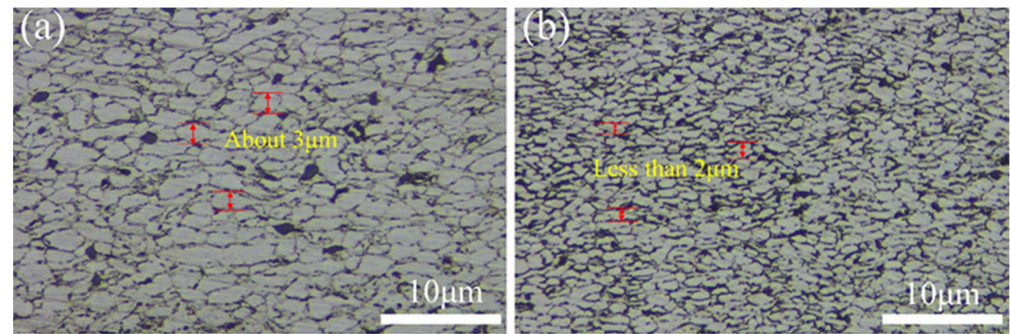
Under different strain rates, the curve coincidence degree of the elastic segment is low, and the change trend is basically consistent. Therefore, the strain rate has a certain influence on the elastic modulus of the 2024Al-Er alloy. At a strain rate of  $600\text{ s}^{-1}$ , the dynamic yield stress of the specimens increases gradually with the increase in Er addition (Figure 8a). When the Er content is 0.6 wt.%, the dynamic yield stress reaches the maximum value of 289.6 MPa and then decreases. When the strain rate increases from  $600\text{ s}^{-1}$  to  $800\text{ s}^{-1}$ , the true stress–true strain curve of the Er/2024Al alloy with different Er contents generally moves upward (Figure 8b), indicating increased stress on the material, and showing the positive strain rate-strengthening effect. When the Er content is 0.6 wt.%, the dynamic yield stress reaches 371.3 MPa, an increase of 28.2% in comparison to that under a  $600\text{ s}^{-1}$  strain rate. It can be seen from the plastic section curve that the dynamic yield stress increases with an increase in strain rate, and there is a trend of strain hardening. It is believed that the alloy with 0.6 wt.%Er has the smallest grain and the highest compactness, which is an important factor for improving the strength. Small grains are more likely to lead to dislocation packing, forming a pinning effect, and exerting the dislocation strengthening mechanism [33].

Figure 9 shows the macro deformation of 0.6 wt.% Er and Er-free specimens under different strain rates. It can be concluded that when the strain rate is  $600\text{ s}^{-1}$ , the deformation degree of the specimen is 32.2%, and there is no obvious macroscopic damage of shear failure in the specimen. When the strain rate reaches  $800\text{ s}^{-1}$ , the deformation degree of the two specimens is 55.3% (0.6 wt.% Er) and 48.2% (Er-free), respectively, and the specimens are seriously damaged. However, from the macroscopic morphology, the damage of the Er-free specimen is more serious, showing the characteristics of brittle fracture.



**Figure 9.** The macro deformation of 0.6 wt.% Er and Er-free specimens under different strain rates.

The microstructure of the 0.6 wt.%Er specimen obtained by light microscopy after dynamic shock loading is presented in Figure 10, and the strain rates are  $600\text{ s}^{-1}$  and  $800\text{ s}^{-1}$  respectively. When preparing the metallographic specimen, it is necessary to cut the specimen along the axis after dynamic compression and take its profile as an observation plane; i.e., the metallographic observation plane shall be parallel to the compression direction.



**Figure 10.** Optical micrographs of 0.6%Er specimens after exposure to different dynamic impact loads: (a)  $600\text{ s}^{-1}$  and (b)  $800\text{ s}^{-1}$ .

It is found that the microstructures of the samples vary with the impact condition. The grains are elongated in a direction perpendicular to that of the impact loading at a lower strain rate ( $600\text{ s}^{-1}$ ). By analyzing the micrographs of the two samples, it is found that with the strain rate and the degree of grain refinement increasing, the elongation increases. The average grain size decreases with the increase in strain rate. This is because when the strain rate increases, the deformation time of the alloy will be shortened, resulting in grain refinement and restrained growth of recrystallized grains. In units of time, the dislocation density in grains increases faster, and the accumulated deformation storage energy is also higher, which will promote the nucleation of recrystallized grains, leading to grain refinement.

The results of scanning electron microscopic (SEM) investigation of the 0.6 wt.%Er specimen after high-strain-rate ( $800\text{ s}^{-1}$ ) deformation under impact loading are presented in Figure 11. Due to instantaneous stress waves, a short standing of high-intensity stress is generated, and it is difficult to transfer the heat generated by the plastic deformation of local regions in time as the process is almost adiabatic. Local softening occurred due to temperature rise, while surrounding regions remained hardened. When further loaded, if the thermal softening conquers the strain rate hardening, the deformation will occur in a strong plastic shear band, forming an adiabatic shear band (ASB) [34].

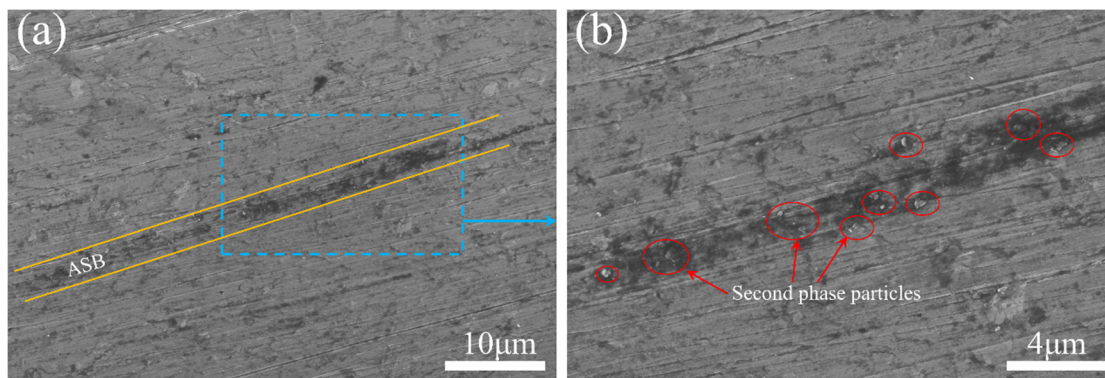


**Figure 11.** (a) The results of scanning electron microscopic investigation of the 0.6%Er specimen after high strain rate ( $800\text{ s}^{-1}$ ) and (b) enlargement of blue wireframe area in Figure 9a.

As is known to all, the formation of localized shear bands is a unique form of microdamage in materials under impact loads, and the formation of shear bands indicates the beginning of material catastrophic failure. It is obvious that the occurrence of the heterogeneous deformation caused the formation of ASB in the alloy (Figure 11a). When excessive thermal softening leads to a decrease in load-carrying capacity and strong strain in the local region along the narrow paths, shear bands will develop. So, the ASBs can be clearly distinguished from other parts of the microstructure under SEM. The second-phase particles in the alloy are also elongated and arranged along the ASB region and become

denser than those outside the shear bands (Figure 11b). The main factor contributing to strain localization is the thermal softening of the matrix in the shear band region. Under the combined action of the pressure of the rigid matrix outside the shear band and the shear flow of the viscoplastic matrix in the shear band region, the arrangement of the second-phase particles in the shear band region is more compact. In a previous study, analogous phenomena were also observed [35].

Figure 12 presents the fracture surfaces of dynamic compression specimens. It can be clearly seen that extensive irregular cleavage planes and some cracks are apparent on the entire fracture surface of the Er-free specimen, as shown in Figure 12a. The cracks expand along the grain boundary, and the grain boundary is obvious. The polyhedron morphology of each grain is similar to the stacking of rock candy. It indicates that the fracture characteristics exhibit quasi-cleavage fracture, resulting in a low strength value of the specimen. Meanwhile, the 0.6 wt.% Er specimen exhibits some dimples, and the number of cracks is reduced. As can be seen in Figure 12b, the morphology of dimple fracture from a 0.6 wt.% Er specimen is obvious, and the dimples are slightly deep and well distributed, which results in higher mechanical properties. However, the morphology of the dimple fracture of the Er-free specimen is not evident, and the dimples are very flat and unevenly distributed. Therefore, the mechanical properties are far inferior to those of the specimen modified with 0.6 wt.% Er. This shows that the addition of Er improves the plasticity and toughness of the 2024Al alloy.

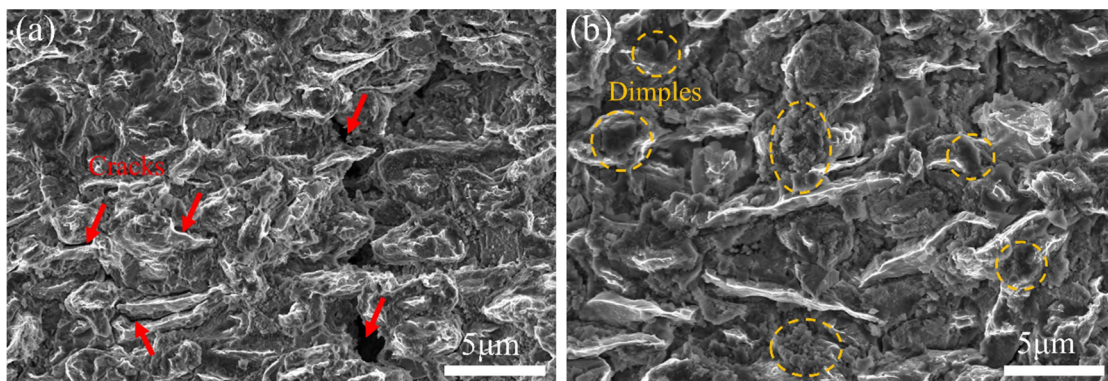


**Figure 12.** The SEM analysis of fracture surfaces of the dynamic compression specimens: (a) Er-free, (b) 0.6 wt.% Er addition.

In general, the propagation of cracks is always present along the direction of the small atomic bonding force. The addition of trace Er makes the microstructure homogenized and refined, which improves the plastic deformation ability of the alloy and hinders crack propagation along the grain boundary [36]. This shows that the addition of Er improves the impact toughness of the alloy. The fracture mode is no longer a simple brittle fracture, and the tendency of ductile fracture begins to appear, which is consistent with the results of a metallographic microstructure and stress–strain curves.

#### 4. Conclusions

An Er/2024Al alloy with different Er contents was prepared by ball milling, cold isostatic pressing, and microwave sintering. The results can be summarized as follows:

(1) When the sintering temperature is 490 °C, the heating rate is 20 °C/min, and the soaking time is 30 min. Thus, the addition of Er can significantly refine the grains of the 2024Al alloy, with the main mechanism being the presence of the  $\text{Al}_3\text{Er}$  phase. This phase acts as a heterogeneous nucleation site, greatly increasing the nucleation rate. Moreover, small  $\text{Al}_3\text{Er}$  particles exert a pinning effect on dislocations and sub-grain boundaries, thereby causing a significant reduction in grain size. The grain size of the 0.6%Er specimen is about 5  $\mu\text{m}$ , which is the optimal value.

(2) The mechanical properties of the 2024Al alloy were improved with the addition of Er. Due to the refinement of the grains, the compactness, strength, and toughness of the alloy were elevated. When the Er content is 0.6%, the compactness and microhardness reach maximum levels, which are 97.6% and 94.5 HV, 1.9% and 2.8% higher than those of the Er-free specimen, respectively. At the same time, the tensile strength and elongation reach the peak at 160.5 MPa and 4.4%, respectively.

(3) At both the strain rates of  $600 \text{ s}^{-1}$  and  $800 \text{ s}^{-1}$ , the dynamic yield stress of the specimens increases gradually with an increase in Er content. For the 0.6 wt.% Er specimen, the dynamic yield stress reaches 371.3 MPa at a strain rate of  $800 \text{ s}^{-1}$ , which is 28.2% higher than that under a  $600 \text{ s}^{-1}$  strain rate. The toughness of the 2024Al-0.6 wt.% Er alloy is enhanced and dimples appear, indicating that the fracture mode changes from brittle fracture to ductile fracture.

The 2024Al alloy has excellent comprehensive mechanical properties, and with the development of the aerospace industry, its requirements for comprehensive performance are constantly increasing. By conducting research on the action effect of rare earth erbium alloying on the microstructure and properties of the 2024 aluminum alloy, it is possible to further optimize the comprehensive performance of the 2024 aluminum alloy, laying the necessary theoretical and practical foundation for the development of advanced high-strength and high-toughness aluminum alloy materials.

**Author Contributions:** Conceptualization, T.Q.; formal analysis, J.Y.; investigation, T.Q., J.Y., and C.B.; writing—original draft preparation, T.Q.; writing—review and editing, B.F.; supervision, J.Z.; funding acquisition, B.F. All authors have read and agreed to the published version of the manuscript.

**Funding:** This research was funded by “The Natural Science Foundation of the Jiangsu Higher Education Institutions of China (23KJB430037)” and “Jiangsu Province Vocational College Teachers Enterprise Practice Training Project (2024QYSJ038)”.

**Data Availability Statement:** The original contributions presented in the study are included in the article; further inquiries can be directed to the corresponding author.

**Conflicts of Interest:** Author J.Z. has been involved as a consultant and expert witness in Wuxi Wanling High Frequency Equipment Manufacturing Co., Ltd. The remaining authors declare that the research was conducted in the absence of any commercial or financial relationships that could be construed as a potential conflict of interest.

## References

- Zhang, H.S.; Yan, M.; Wang, H.Y.; Shen, L.T.; Dai, L.H. Determination of dynamic shear strength of 2024 aluminum alloy under shock compression. *AIP Adv.* **2016**, *6*, 045309. [\[CrossRef\]](#)
- Gautam, A.; Sarkar, P.K.; Jangid, R. Ductile and Fatigue Behaviour Estimation of Lightweight High-Strength Al 2024. *Mater. Today Proc.* **2018**, *5*, 7873–7881. [\[CrossRef\]](#)
- Rohatgi, P.K.; Kumar, P.A.; Chelliah, N.M.; Rajan, T.P.D. Solidification processing of cast metal matrix composites over the last 50 years and opportunities for the future. *JOM* **2020**, *72*, 2912–2926. [\[CrossRef\]](#)
- Nazree, M.; Nabilla, S.; Che, Z. The effect of microwave sintering time to PM aluminum alloys. *Appl. Mech. Mater.* **2015**, *754–755*, 240–244.
- Wang, H.; Tang, F.; Li, G.; Zhang, D.; Liu, M.; Kai, X. Microstructure and properties of  $\text{B}_4\text{C}_p/\text{Al}$  composite prepared by microwave sintering with low temperature. *Mater. Res. Express* **2020**, *7*, 096511. [\[CrossRef\]](#)
- Han, Z.; Xu, L.; Guo, S.; Wu, Q.; Zhang, L.; Liu, J. Study on the microwave sintering characteristics of spherical tin-silver alloy powder. *Mater. Res. Express* **2019**, *6*, 1265k7. [\[CrossRef\]](#)
- Liu, J.Q.; Wang, H.M.; Li, G.R.; Su, W.X.; Zhang, Z.B.; Zhou, Z.C.; Dong, C. Microstructure and improved plasticity of  $(\text{FeCoNi}_{1.5}\text{CrCu})_p/\text{Al}$  composites subject to adjusted deep cryogenic treatment (DCT). *J. Alloys Compd.* **2022**, *895*, 162690. [\[CrossRef\]](#)
- Liu, J.Q.; Wang, H.M.; Huang, Z.H.; Ma, Z.; Li, G.; Zhou, P. Enhanced strength-ductility synergy of aging treated  $(\text{FeCoNi}_{1.5}\text{CrCu})_p/2024\text{Al}$  composite. *J. Alloys Compd.* **2022**, *929*, 167372. [\[CrossRef\]](#)
- Gaurava, A.; Satpala, S. Influence of rare earth addition on the properties of AA6351 hybrid composites. *J. Eng. Res.* **2021**, *9*, 253–268.
- Nazarov, S.; Rossi, S.; Bison, P. Influence of Rare Earths Addition on the Properties of Al–Li Alloys. *Phys. Met. Metallogr.* **2019**, *120*, 402–409. [\[CrossRef\]](#)

11. Nogita, K.; McDonald, S.D.; Dahle, A.K. Eutectic modification of Al-Si alloys with rare earth metals. *Mater. Trans.* **2004**, *45*, 323–326. [[CrossRef](#)]
12. Tsai, Y.C.; Chou, C.Y.; Lee, S.L.; Lin, C.K.; Lin, J.C.; Lim, S.W. Effect of trace La addition on the microstructures and mechanical properties of A356 (Al-7Si-0.35Mg) aluminum alloys. *J. Alloys Compd.* **2009**, *487*, 157–162. [[CrossRef](#)]
13. Zhong, T.; Zeng, G.; Xiao, M.; Qin, S.; Wan, Y. Effect of Rare Earth Ce on Microstructure and Properties of 3003 Aluminum Alloy. *Rare Met. Cem. Carbides* **2019**, *33–36*, 41.
14. Ding, W.W.; Zhao, X.Y.; Chen, T.L. Effect of rare earth Y and Al-Ti-B master alloy on the microstructure and mechanical properties of 6063 aluminum alloy. *J. Alloys Compd.* **2020**, *830*, 154685. [[CrossRef](#)]
15. Shi, Z.M.; Wang, Q.; Zhao, G.; Zhang, R. Effects of Erbium modification on the microstructure and mechanical properties of A356 aluminum alloys. *Mater. Sci. Eng.* **2015**, *A626*, 102–107. [[CrossRef](#)]
16. Li, Q.; Xia, T.; Lan, Y.; Li, P. Effects of rare earth Er addition on the microstructure and mechanical properties of Al-20Si alloy. *Mater. Sci. Eng.* **2013**, *A588*, 97–102. [[CrossRef](#)]
17. Nie, Z.; Jin, T.; Zou, J.; Fu, J.; Yang, J.; Zuo, T. Development on research of advanced rare-earth aluminum alloy. *Trans. Nonferrous Met. Soc. China* **2003**, *13*, 509–514.
18. Yang, J.; Nie, Z.; Jin, T.; Xu, G.; Fu, J.; Ruan, H.; Zuo, T. Effect of trace earth element Er on high pure Al. *Trans. Nonferrous Met. Soc. China* **2003**, *13*, 1035–1039.
19. Yu, Y.; Shi, Y.; Xia, Z. Effect of rare earth element Er on microstructure and properties of Al-Si-Cu solder alloy. *Beijing Gongye Daxue Xuebao* **2008**, *32*, 1148–1152.
20. Xing, Z.; Nie, Z.; Ji, X.; Wang, X.; Zou, J. Effect of trace element erbium and manganese on microstructure and properties of Al-Mg alloy. *Rare Met. Mater. Eng.* **2006**, *35*, 1979–1982.
21. Wu, H.; Wen, S.P.; Huang, H.; Li, B.; Wu, X.; Gao, K.; Wang, W.; Nie, Z. Effects of homogenization on precipitation of Al<sub>3</sub>(Er, Zr) particles and recrystallization behavior in a new type Al-Zn-Mg-Er-Zr alloy. *Mater. Sci. Eng. A* **2017**, *689*, 313–322. [[CrossRef](#)]
22. Sun, W. *Behavior of Rare Earth in Aluminum Alloys*; Press of Weapon Industry: Beijing, China, 1992.
23. Hu, X.; Jiang, F.; Ai, F.; Yan, H. Effects of rare earth Er additions on microstructure development and mechanical properties of die-cast ADC12 aluminum alloy. *J. Alloys Compd.* **2012**, *538*, 21–27. [[CrossRef](#)]
24. Colombo, M.; Gariboldi, E.; Morri, A. Er addition to Al-Si-Mg-based casting alloy: Effects on microstructure, room and high temperature mechanical properties. *J. Alloys Compd.* **2017**, *708*, 1234–1244. [[CrossRef](#)]
25. Li, Y.; Liu, Z.; Ma, F.; Xia, Q. Phase constitution and growth manner at grain boundary in Al-Cu-Mg-Ag-Er alloy. *Rare Met. Mater. Eng.* **2008**, *37*, 1019–1022.
26. Nie, Z.R.; Fu, J.B.; Zou, J.X.; Jin, T.N.; Yang, J.J.; Xu, G.F.; Ruan, H.Q.; Zuo, T.Y. Advanced Aluminum Alloys Containing Rare-earth Erbium. *Mater. Forum* **2005**, *28*, 197–201.
27. Zou, M.; Ge, Z.; Qi, L.; Zhou, X.; Wei, X.; Zhang, J.; Chen, J. Effect of erbium (Er) on the hot cracking behaviour of Al-5Cu alloy. *Mater. Sci. Technol.* **2011**, *17*, 1–36. [[CrossRef](#)]
28. Wang, H.; Ren, W.; Li, G.; Wen, H.; Wang, C.; Chen, J.; Zhao, Y.; Chen, G.; Kai, X. Microstructure and properties of FeCoNi<sub>1.5</sub>CrCu/2024Al composites prepared by microwave sintering. *Mater. Sci. Eng. A* **2021**, *801*, 140406. [[CrossRef](#)]
29. Lei, X.; Zhang, Z.; Dong, H.; Wang, C.; Du, X. Effect of erbium on microstructure and mechanical properties of Al-Si-Mg-Cu alloy. *Mater. Und Werkst.* **2020**, *51*, 1389–1397. [[CrossRef](#)]
30. Wang, J.; Dong, N.; Ma, H. Study on high speed impact deformation behaviors of Mg-1Al-4Y by SHPB. *Mater. Res. Express* **2020**, *7*, 116506. [[CrossRef](#)]
31. Xie, W.; Wang, H. Research on dynamic mechanical properties of SiC<sub>p</sub>/2024Al composites prepared by hot-pressing sintering. *Powder Metall. Ind.* **2021**, *31*, 47–51.
32. Cai, Z.; Ji, Z.; Cui, J.; Tian, W. Deformation behaviors and microstructure evolution of 60Al-30Fe-10Bi alloy under high speed impact. *Powder Metall. Technol.* **2017**, *35*, 352–357.
33. Casati, R.; Vedani, M. Metal Matrix Composites Reinforced by Nano-Particles-A Review. *Metals* **2014**, *4*, 65–83. [[CrossRef](#)]
34. Zhang, X.; Li, H.; Li, H.; Gao, H.; Gao, Z.-G.; Liu, Y.; Liu, B. Dynamic property evaluation of aluminum alloy 2519A by split Hopkinson pressure bar. *Trans. Nonferrous Met. Soc. China* **2008**, *18*, 1–5. [[CrossRef](#)]
35. Odeshi, A.G.; Owolabi, G.M.; Singh, M.N.K.; Bassim, M.N. Dynamic shear band formation in Aluminum 6061-T6 and Aluminum 6061-T6/Al<sub>2</sub>O<sub>3</sub> composites. *Mat. Sci. Eng. A Struct.* **2007**, *457*, 114–119.
36. Liu, L.; Liu, L.; Cao, F.; Yang, T.; Yin, P.Z. Effect of Er element on impact deformation and failure behaviors of 7xxx series aluminum alloy. *Ordnance Mater. Sci. Eng.* **2020**, *43*, 125–130.

**Disclaimer/Publisher’s Note:** The statements, opinions and data contained in all publications are solely those of the individual author(s) and contributor(s) and not of MDPI and/or the editor(s). MDPI and/or the editor(s) disclaim responsibility for any injury to people or property resulting from any ideas, methods, instructions or products referred to in the content.